View metadata, citation and similar papers at core.ac.uk

brought to you by CORE

provided by Online Research Database In Technology

DTU Library

The Dimensioning Sea Loads (DIMSELO) project

Paper

Pierella, Fabio; Bredmose, Henrik; De Vaal, Jacobus B.; Eliassen, Lene; Krokstad, Jørgen; Anders Nygaard, Tor; Oggiano, Luca; Stenbro, Roy

Published in:
Journal of Physics: Conference Series

Link to article, DOI:
10.1088/1742-6596/1104/1/012037

Publication date:
2018

Document Version
Publisher's PDF, also known as Version of record

Link back to DTU Orbit

Citation (APA):
Pierella, F., Bredmose, H., De Vaal, J. B., Eliassen, L., Krokstad, J., Anders Nygaard, T., ... Stenbro, R. (2018). The Dimensioning Sea Loads (DIMSELO) project: Paper. Journal of Physics: Conference Series, 1104(1), [012037]. DOI: 10.1088/1742-6596/1104/1/012037

General rights
Copyright and moral rights for the publications made accessible in the public portal are retained by the authors and/or other copyright owners and it is a condition of accessing publications that users recognise and abide by the legal requirements associated with these rights.

- Users may download and print one copy of any publication from the public portal for the purpose of private study or research.
- You may not further distribute the material or use it for any profit-making activity or commercial gain
- You may freely distribute the URL identifying the publication in the public portal

If you believe that this document breaches copyright please contact us providing details, and we will remove access to the work immediately and investigate your claim.

Journal of Physics: Conference Series

PAPER • **OPEN ACCESS**

The Dimensioning Sea Loads (DIMSELO) project

To cite this article: Fabio Pierella *et al* 2018 *J. Phys.: Conf. Ser.* **1104** 012037

View the article online for updates and enhancements.

IOP ebooks™

Bringing you innovative digital publishing with leading voices to create your essential collection of books in STEM research.

Start exploring the collection - download the first chapter of every title for free.

This content was downloaded from IP address 192.38.67.116 on 09/11/2018 at 08:58

The Dimensioning Sea Loads (DIMSELO) project

Fabio Pierella[12], Henrik Bredmose[2], Jacobus B. De Vaal[1], Lene Eliassen [3], Jørgen Krokstad[3], Tor Anders Nygaard[1], Luca Oggiano [1] and Roy Stenbro[1]

[1] Institute for Energy Technology (IFE), 2008 Kjeller, Norway
[2] Technical University of Denmark (DTU), 2800, Kgs. Lyngby, Denmark
[3] Norwegian University of Science and Technology (NTNU), 7491, Trondheim, Norway

E-mail: roy.stenbro@ife.no

Abstract. DIMSELO is a Competence Building for Industry project (KPN), granted by the Norwegian Research Council under the ENERGIX program, which ran from 2013 to 2017. The project's objective was to quantify the consequences of using advanced sea loads modeling in integrated simulations of offshore wind turbines in shallow to intermediate waters. During the project, engineering hydrodynamics load and wave kinematics models of increasing complexity and fidelity were chosen from the literature and implemented. The effect of different model combinations on the substructure loads was was tested for three reference turbines: a DTU 10 MW rotor positioned on a monopile at a water depth of $h = 25\ m$, on a second monopile at $h = 35\ m$ and on a jacket, also at $h = 35\ m$. In this paper, the fatigue loads in a production case for the $h = 25\ m$ monopile was calculated via three different load models: the well-known Morison model, the Rainey nonlinear force model and the McCamy-Fuchs linear diffraction model. The models were coupled to kinematics coming both from linear irregular waves and second order irregular waves. The comparison showed that using the McCamy-Fuchs diffraction theory reduced the predicted fatigue damage by 15% with respect to a base case where the Morison load model was used. Nonlinear wave kinematics and nonlinear force models influenced the force calculations but did not alter the total fatigue damage, since the load cases with high wave steepness were less likely to happen.

In parallel to the research on engineering models, detailed wave loads models were also developed during DIMSELO. By means of CFD, it was possible to reproduce experimental time series of wave loads on a cylinder induced by regular and irregular nearly-breaking waves. Also, a spectral solver for the fast resolution of the fully nonlinear diffraction problem was devised at DTU during DIMSELO. The solver, which showed encouraging results in the preliminary testing, can be coupled to any nonlinear kinematics solver to calculate the force on a cylinder retaining full nonlinearity and diffraction.

1. Introduction

DIMSELO is a Competence Building for Industry project (KPN) granted by the Norwegian Research Council under the ENERGIX program. It ran from 2013 to 2017, aimed at improving sea loads modeling in integrated simulations of offshore wind turbines in shallow to intermediate waters.

Many new offshore wind farms are nowadays built at $30 - 40\ m$ water depth. This is economically feasible since the increase in substructure manufacturing costs is compensated by higher energy availability further from the coast. The most economic solution is still to install turbines on top of slender piles, fixed on the sea bottom.

Content from this work may be used under the terms of the Creative Commons Attribution 3.0 licence. Any further distribution of this work must maintain attribution to the author(s) and the title of the work, journal citation and DOI.
Published under licence by IOP Publishing Ltd

However, the standard design engineering practice is largely based on models inherited from the offshore oil industry, where large structures in deep waters were designed. Hence, they can be unreliable when applied to simulate slender piles. In the standard modeling approach used for fatigue load cases, waves are represented as an irregular realization of linear (1^{st} order) waves. However, at intermediate depths nonlinearity cannot be neglected, and a linear wave description is inaccurate. Various nonlinear models exist, from weakly linear second order formulations [1] to fully nonlinear ones [2], but the number of calculations required to run a nonlinear computation is many order of magnitudes higher than for a linear state.

In the standard practice, the wave kinematics is then translated into loads by means of simple methods, like the Morison semi-empirical model [3]. In reality, a large monopile will diffract incoming waves with wavelength comparabe with its diameter, which leads to a reduction on the total horizontal force. In linear waves, McCamy and Fuchs derived an exact result for the cylinder diffraction problem [4]. Comparisons between the two models shows that the Morison formulation overestimates the loads significantly for wavelengths smaller than 5 cylinder diameters. Today, only some aeroelastic codes incorporate linear diffraction theory for the hydrodynamics loads [5][6].

For extreme loads, the designer uses the 50 year significant wave height $H_{S,50}$ relative to a three hour sea state to simulate an extreme sea state. To calculate the extreme structural response, standard practices [7] suggest to perform one hour simulations with a corrected wave height ($H_{S,50,1hr} = 1.09 \cdot H_{S,50,3hr}$). However, 10 minute realizations can be accepted if a deterministic exteme wave is embedded in the simulation, with an extreme wave height of $H_{50} = 1.86 H_{S,50}$. This is an approximated value calculated on the hypothesis that the wave peaks follow a Rayleigh distribution. This procedure is also called *hard embedment*. The design force, calculated via the Morison model, is then taken as the average of the maximum forces from the different realizations.

However, the 1.86 factor is a nonconservative approximation, and in practice higher peaks can be observed in a three hour realization. Therefore, the hard embedment method can be regarded to be as good as using a series of regular nonlinear waves. To overcome this limitation, designers can run three hour simulations using the 50 year sea state, and then substitute the highest linear wave with a nonlinear wave (*soft embedment*). The extreme responses are then fitted to a Gumbel distribution, and the extreme load extrapolated to the desired return time [8]. This approach is much more physically correct, but more computationally intesive, and is not implemented in any aeroelastic code.

Moreover, when large extreme waves hit a turbine, higher order forcing can be transferred to the higher structural eigenmodes. Although the Morison model can underestimate this nonlinear behavior, it is still the only choice in many aeroelastic codes.

To conclude, it is today accepted knowledge that using linear waves and the Morison equation is a crude simplification of reality when the inertial terms have a certain degree of nonlinearity and diffraction. In this situation, complex models allow for a better reproduction of reality. However, the increase in accuracy with complex models comes with additional computational cost. While it is vital to make such kind of decisions, it is hard to quantify the error that a designer is making when choosing a simpler model over a more complex one. The objective of DIMSELO is to fill this gap, and help the designer choose the most appropriate combination of wave kinematics and wave load models for the load estimations.

2. Activities in DIMSELO

The Institute for Energy Technology (IFE) in Oslo was the main applicant and project manager of the DIMSELO project. Statoil and Statkraft participated as industrial partners, while DTU and NTNU were appointed as academic partners.

The project included different related activities:

- Sea loads modeling

- Wave kinematics modeling
- Wind field modeling
- Quantify effects of different models on dimensioning loads

2.1. Sea Loads and Wave kinematics modeling
Two main categories of hydrodynamic models were analyzed in parallel: engineering and fully-resolved models. Engineering models are used to calculate the extensive set of load cases that are necessary to design a wind turbine. Hence the focus was set on finding and implementing simple models that retained as much physics as possible. Fully resolved models are physically accurate but computationally expensive to run. They were therefore used as benchmark for engineering models or to analyze single complex cases.

In a first phase, the literature was analyzed to find engineering models of different complexity and accuracy. Afterwards, a correct mix of models was chosen and then implemented as modules into 3DFloat, an aeroelastic software developed in-house at IFE [9]. In the third phase, the consequences on the design load calculations due to the different models was assessed by performing design load calculations on three structures via the abovementioned 3DFloat package.

To take into account nonlinearity in wave kinematics for fatigue calculations, the Sharma and Dean second-order irregular wave theory model was chosen [1]. A Fast Fourier Transform (FFT) in the $k-$space domain was used to speed up the implementation of the otherwise computationally intensive model.

To improve the representation of the kinematics in extreme load cases, a procedure for seamlessly embedding streamfunction waves into a linear wave realizaton was invented and implemented. The algorithm makes use of the Hilbert transform to calculate a suitable period and amplitude of a regular wave to replace an extreme event in the linear realization [10].

For what concerns fatigue loads from linear waves hitting large monopiles, the already mentioned McCamy-Fuchs diffraction theory was implemented. To improve the calculation of nonlinear extreme wave loads, the Rainey slender body model [11] was included in 3DFloat. The Rainey model can be seen as an extension to the Morison force model. However, being based on an energy conservation approach, retains a larger amount of physics.

The effect of the different computational models on the design loads of wind turbines was analyzed by means of aeroelastic computations. Three structures were developed ad-hoc for the DIMSELO project, to support a 10 MW DTU rotor positioned at different water depths (h):

- Monopile at $h = 25\ m$
- Monopile at $h = 35\ m$
- Jacket at $h = 35\ m$

In the results section, we will present results for the fatigue design of the monopile at $h = 25\ m$. The rest of the results will be published in a dedicated report.

On the parallel track concerning fully-resolved models, two main activities were undertaken in DIMSELO. In the first activity, DTU worked on the development of a so called *higher-order spectral model* to allow fully nonlinear force computations with no compromise on diffraction. The objective was filling in the space between the McCamy-Fuchs force model, that can handle diffraction but not nonlinear waves, and the Rainey model that can work with any wave kinematics, but still models the body as a slender beam [12]. The core of the model is represented by the formulation of the linear and nonlinear diffraction potential by the cylinder by series expansion of appropriate Bessel functions. The incident wave field can be calculated either by closed formulations or by nonlinear solvers like OceanWave3D [2]. Some preliminary results are presented in the next section.

In parallel, IFE developed CFD models of waves impacts on monopiles via the Star-CCM+ package. Numerical reproduction of experiments on wave forcing on a circular stiff cylinder by regular and irregular waves on a sloping bottom allowed a very accurate reproduction of the inline force and of the flow patterns [13, 14, 15].

2.2. Wind Field Modeling

The modeling of aerodynamic loads was also an important part of DIMSELO. The main challenge was to analyze the effect of the turbulence modeling in the design of large rotors. Two different methods are today used to model the turbulent wind field: the Kaimal model and the Mann model. They are both recommended by the offshore wind standards, and both have the same one-point spectrum. The difference is in how the spatial coherence is modelled. The Kaimal model uses an exponential model, while the Mann model is a linearized version of the Navier-Stokes where turbulence is created by the shear of the vertical wind profile.

In the first part of the project, the vertical coherence in stable conditions was characterized experimentally through the FINO offshore met mast. It was observed that the Mann spectrum had a more realistic modelling of the coherence than the exponential model in Kaimal [16]. The difference between the two models increased with greater vertical separation distances, which makes it of special importance for today's large offshore wind turbine rotors.

In a second part, the sensitivity of rotor size and choice of turbulence model on the fatigue loads on the floating offshore wind turbines was investigated [17]. The two turbines had similar semi-submersible substructures but one used a 5 MW NREL rotor and the other used the DTU 10 MW[18]. For both turbines, the choice of turbulence models has the greatest impact on the fatigue of the mooring lines, especially due to the surge contribution. The Kaimal model gave the highest fatigue damage of the mooring line for both wind turbines, with the larges difference for the 10 MW turbine. It was also seen that the yaw motion was larger for the Mann model than for the Kaimal model, which makes the turbulence modeling critical in cases where the fatigue damage is sensitive to yaw.

Proper Orthogonal Decomposition (POD) method was then used to visualize the spatial coherent structures in the two turbulence models [19]. The lowest POD modes, which contain the most kinetic energy and are the most important for the turbine response, were very different for the two turbulence models. The coherent structures from the Kaimal model had a more symmetric shapes while the ones from the Mann model were stretched in the horizontal direction.

3. Main results

3.1. Fatigue calculation on a monopile at $h = 25$ m water depth

In the following section, we will quantify the effects of different combination of wave loads models on the design fatigue loads of an offshore bottom-fixed wind turbine, positioned on a monopile at 25 m water depth.

3.1.1. Tower and pile The soil conditions for the monopile design were provided by Statoil, on the base of their experience with North Sea installations. It was decided to select a pile with a penetration of $p = 35$ m and a thickness of $t = 0.08$ m. From now on, the coordinates of points are given with respect to a right-handed coordinate system positioned at the mean sea level (MSL), with z pointing upwards, x in the direction of the wind and y sideways.

The soil stiffnesses, taken as base of the design, are reported in Table 1. The soil effect was simulated via $p - y$ curves, and the springs for the current setup were calculated by means of the API/DNV methodology [20]. The distribution and the elastic constants of the springs are summarized in Table 2. At each level, the same stiffness was applied both in the x and y direction. The translation along the z axis and the yaw rotation of the bottom node ($z = -60$ m) were locked.

Soil Depth $[m]$	Cu $[kPa]$
0 - 5	75
5 - 10	125
10 +	200

Table 1: Soil stiffness for a typical Northern Sea location. The depth is measured from the mudline, which is positioned at $z = -25\ m$

Spring	$z[m]$	$k_1[N/m]$	$k_2[N/m]$	$k_3[N/m]$	$F^1_{max}[N]$	$F^2_{max}[N]$	$F^2_{max}[N]$
0	-26.25	2.84e+07	2.50e+07	7.96e+07	3.16e+05	4.55e+05	6.32e+05
1	-28.75	3.47e+07	3.05e+07	9.71e+07	3.85e+05	5.55e+05	7.70e+05
2	-31.25	7.47e+07	6.57e+07	2.09e+08	6.64e+05	9.56e+05	1.33e+06
3	-33.75	8.34e+07	7.34e+07	2.34e+08	7.42e+05	1.07e+06	1.48e+06
4	-36.25	1.04e+08	9.18e+07	2.92e+08	1.16e+06	1.67e+06	2.32e+06
5	-38.75	1.69e+08	1.49e+08	4.73e+08	1.25e+06	1.80e+06	2.50e+06
6	-41.25	1.81e+08	1.59e+08	5.07e+08	1.34e+06	1.93e+06	2.68e+06
7	-43.75	1.93e+08	1.70e+08	5.41e+08	1.43e+06	2.06e+06	2.86e+06
8	-46.25	2.06e+08	1.81e+08	5.76e+08	1.52e+06	2.19e+06	3.05e+06
9	-48.75	2.18e+08	1.92e+08	6.10e+08	1.61e+06	2.32e+06	3.23e+06
10	-51.25	2.30e+08	2.03e+08	6.45e+08	1.71e+06	2.46e+06	3.41e+06
11	-53.75	2.42e+08	2.13e+08	6.79e+08	1.80e+06	2.59e+06	3.59e+06
12	-56.25	2.55e+08	2.24e+08	7.13e+08	1.89e+06	2.72e+06	3.77e+06
13	-58.75	2.67e+08	2.35e+08	7.48e+08	1.98e+06	2.85e+06	3.96e+06

Table 2: Spring distribution on the 25 m monopile. The F_max values mark the upper boundaries for the validity of the different spring constants.

The monopile was designed to have an eigenfrequency of $f = 0.23\ Hz$ in the fore-aft first bending mode. The bending resistance of the monopile was designed to withstand the large thrust of the 10 MW rotor. The characteristics of the pile and of the tower are summarized in Table 3. The weight of the transition piece was simulated by a point force of 4.59 MN applied at $z = 19\ m$, oriented towards the negative z direction. The yaw bearing element and the nacelle were then positioned on top of the tower, resulting in a total hub height of 119.0 m above MSL.

Both pile and tower were considered as made of steel, with a Young modulus of $E = 210\ GPa$, a torsional stiffness of $G = 80\ GPa$ and a density of $\rho = 7800\ kg/m^3$. Two dampers were positioned at the mudline, one in the x and one in the y direction, to achieve 1.5% of the critical damping of the fore-aft tower first eigenmode.

Reference	$z_1[m]$	$z_2[m]$	$D_1[m]$	$D_2[m]$	$t_1[m]$	$t_2[m]$	$n_{el}[-]$
Pile below mudline	-60	-25	9.0	9.0	0.08	0.08	28
Pile above mudline	-25	0	9.0	9.0	0.08	0.08	10
Pile above water	0	11.5	9.0	9.0	0.08	0.038	4
Up to transition piece	11.5	19.0	9.0	8.75	0.038	0.036	2
Tower	11.5	115.63	8.75	6.25	0.038	0.02	18

Table 3: Structural Characteristics of the pile. For each section, we report the diameters, the steel thickness, and the number of beam elements by which it was discretized.

3.1.2. Rotor and controller The DTU 10 MW rotor was used in the computations. The rotor has a diameter of $D = 178.3\ m$, with the abovementioned hub height of $h_{hub} = 119.0\ m$. The rated rotor speed is 9.6 rpm, leading to a maximum tip speed of 90 m/s. The blade root is shaped as a cylinder, while the lift-generating sections of the blade belong to the FFA-W3 airfoil series, with different thicknesses. A maximum rotor thrust of $T = 1500\ kN$ ($C_T = 0.82$) was achieved for $V_{wind} = 12\ m/s$, above which the turbine outputs the rated power of $P = 10\ MW$.

The rotor geometry is plotted in Figure 1a. The twist goes from a maximum of roughly 14° to almost zero at the blade tip. Some rotor material properties are reported in Figure 1b. The value EA is the Young modulus multiplied by the cross sectional area, while GJ is the torsional stiffness. The linear density ρ_l is the amount of mass per meter of blade length. A thorough description of the rotor and of the aerodynamic characteristics of the airfoils can be found in the relative DTU report [18].

The rotor was discretized via 34 beam elements, of roughly 3 m each. Further details on the rotor aeroelastic model will be available in the final DIMSELO report.

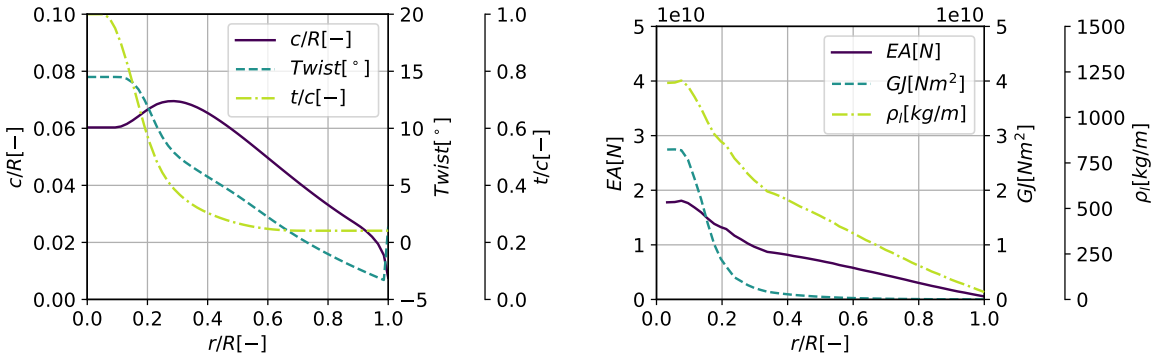

(a) Rotor geometry.

(b) Rotor material properties.

Figure 1: The total blade length is $R = 89.15\ m$. The twist is given in degrees.

The generator torque and blade pitch were regulated via the DTU Wind Energy controller. It features two main control zones, one of partial load for speeds lower than 12 m/s, and one of full load where the torque is controlled via blade pitching. The controller source code [21] was compiled into a DLL and then interfaced with the aeroelastic code.

3.1.3. Aeroelastic Code The aeroelastic calculations were performed in time domain via the aeroelastic code *3DFloat*. It is a finite element code, with Euler-Bernoulli beams with 12 degrees of freedom. The time integration of the equation was performed via the implicit generalized-alpha scheme, with a time step of $\Delta t = 0.01\ s$. The rotor loads were calculated via the classic Blade Element Method [22]. The flow velocity reduction due to tower shadow was calculated via a simple potential flow model.

3.1.4. Met-Ocean conditions The monopile was tested for fatigue loads. Statoil provided a simplified joint probability distribution of significant wave height H_S and peak period T_P, plotted in Figure 2, deemed suitable for preliminary studies. The conditional wind speed at 100 m height, U_{100}, is summarized Table 4. For each sea state, one JONSWAP spectrum was generated, and a 1 hour aeroelastic compuation was performed. For the spectrum, a high cut-off frequency of $3T_P$ was used, while the timestep in the frequency discretization was $\mathrm{d}f = 1/3600.\ Hz$, to avoid repetition of the waves.

The directional distribution of the waves was calculated via a cosine squared function, see paragraph 3.5.8.7 of the DNV recommended practices [23]. For each sea state, two different wave spreading were considered: a multidirectional sea ($s = 5$), and an almost unidirectional sea ($s = 20$).

The turbulent wind inbox was calculated according to Mann's uniform shear turbulence model [24]. A reference wind speed of $V_{ref} = 37.5\ m/s$ together with a C turbulence class was used to calculate the input parameters to Mann's model. The longitudinal turbulence scale parameter was set to $\Gamma_1 = 42\ m$, while the lateral and upward components were set respectively to $\sigma_1 = 0.7$ and $\sigma_2 = 0.5$. The turbulent length scale in the Mann model was set as $L = 0.7\Gamma_1$. The turbulence box had $N_x = 65536$ cells along the wind direction, and $N_y \times N_z = 32 \times 32$ cells in the cross-wind plane, with a cell size of $\Delta y = \Delta z = 7\ m$. In the wind direction, the cell size was $\Delta x = U \cdot T/65536$, where the total simulation time was $T = 1\ hr$ and U was the mean wind speed in the load case. The mean wind velocity U was taken from Table 4 and corrected, according to power law with exponent $\alpha = 0.2$, for the effective hub height of $h_{hub} = 119\ m$. For further details on the calculation of the other constants, refer to annex B of the IEC standards [25] and to the final DIMSELO report, currently under preparation.

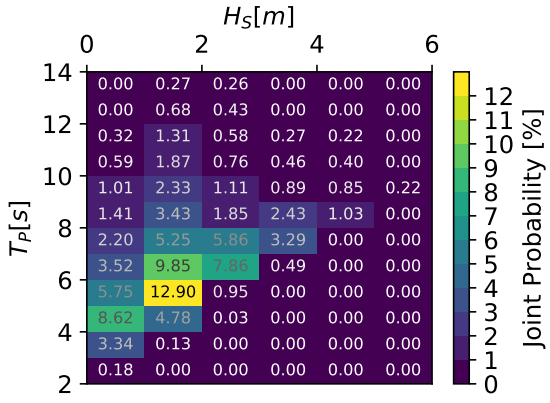

Figure 2: H_S and T_P distribution.

$H_S[m]$	$U_{100}[m/s]$
0.5	5.8
1.5	9.1
2.5	13.5
3.5	17.6
4.5	21.0
5.5	23.8

Table 4: Wind speed at 100 m height U_{100}, conditional on the significant wave height H_S

3.1.5. Combinations of hydrodynamic models For the fatigue calculations, two wave kinematics models were tested: linear waves and second-order irregular waves [1].

Three hydrodynamic loads models were taken under consideration. The well-known semi-empirical Morison force model [3] considers the body as slender. It states that the mass forces, due to the alternate acceleration of the fluid surrounding the body, and the viscous forces, due to the separation of the boundary layer on the cylinder surface, can simply be superimposed. The distributed force on a fixed beam immersed in an oscillating flow is therefore:

$$\mathrm{d}F = \rho A C_M \vec{a}\,\mathrm{d}z + 0.5\rho L|\vec{u}|\vec{u}\,\mathrm{d}z \tag{1}$$

where $\mathrm{d}F$ is the distributed force on the cylinder, ρ is the fluid density, A is the member cross-sectional area, $\vec{a}$ is the fluid acceleration, L is the member size, perpendicular to the fluid flow direction, and $\vec{u}$ is the fluid velocity.

Two other force models were made available: the McCamy-Fuchs and the Rainey model [11]. For a cylindrical surface piercing column, the Rainey force model adds two additional inertial terms to the Morison equation. One, called the axial divergence term, takes into account the fact that the cylinder is nonslender in the vertical direction [26]. The second is a local diffraction force at the intersection between the wave surface and the cylinder, which takes into account the energy added to the fluid due to the rate of change of the submerged height of the cylinder [27].

3.1.6. Results Fatigue calculations For each combination of H_S and T_P, ten simulations were run, as in Table 5. The simulations were performed in accordance with load case number 1.2 from the IEC-61400 standard document [25]. This means the turbines are operating, and the wind has normal turbulence.

LC	Wave Kinematics	Force Model	Wave Spread $[s]$	$\hat{D}^F_{mudl}$	$\hat{D}^M_{broot}$
1	1^{st}-order	Morison	20	1.00	1.00
2	1^{st}-order	Rainey	20	0.99	1.01
3	1^{st}-order	McCamy-Fuchs	20	0.85	1.00
4	2^{nd}-order	Morison	20	0.98	1.00
5	2^{nd}-order	Rainey	20	1.01	1.00
6	1^{st}-order	Morison	5	0.80	0.98
7	1^{st}-order	Rainey	5	0.80	0.99
8	1^{st}-order	McCamy-Fuchs	5	0.68	0.98
9	2^{nd}-order	Morison	5	0.78	0.99
10	2^{nd}-order	Rainey	5	0.80	1.00

Table 5: Combination of models used to run the simulations in the different load cases (LC). The value s in wave spread is the exponent of the cosine-square directional distribution [23]. In column 5, the total damage caused on the pile by the x-wise force at the mudline is summarized. In column 6, the total damage caused on the blade by the flapwise blade root moment is summarized. The computations with the Morison load model and linear waves (LC = 1) were used as a reference case, therefore the value of the total damage is set to $\hat{D} = 1.00$.

The objective is to compare the predicted total damage to the turbine component when using different wave kinematics and wave load models. Hence, random fatigue loads were transformed to damage equivalent loads (DEL), by applying a rainflow counting algorithm and the Palmgren-Miner rule for fatigue accumulation [22]. From theory, we know that the total damage to a component ($\hat{D}$) is, in first approximation, proportional to the DEL to the power of the Wöhler exponent m:

$$\hat{D} \propto DEL^m \tag{2}$$

The lifetime, on the other hand, is inversely proportional to the total damage $\hat{D}$.

During the aeroelastic simulations, the loads were sampled at two representative locations: the x-wise force at the base of the pile (mudline) and the flapwise moment at the root of one of the blades. The DEL^m was calculated at these two locations, and the value achieved with linear waves and the Morison load model (load case 1, or in short LC1), was used as the reference total damage. To calculate the DEL, the steel Wöhler exponent ($m = 3$) was used. The results are summarized in Table 5.

For what concerns quasi-unidirectional 1^{st}-order waves ($s = 20$), the Rainey force model does not give significantly different predictions than the Morison model. This is visible also in figure Figure 3a, where exceedance probabilities for the peaks in the in-line force at the mudline are presented. Since the magnitude of the higher order terms in the Rainey force model are proportional to the wave steepness, they become almost negligible in linear waves. The tabled results also show that introducing diffraction in the calculation implies a reduction of the damage by 15%. In fact, according to the McCamy-Fuchs theory, waves with wavelength shorter than $5D$ are partially or totally scattered by the structure. In a water depth of $h = 20\ m$, this wave length corresponds to a period of $T = 5.4\ s$. As Figure 2 points out, a significant amount of energy is concentrated in this range, hence the damage reduction in LC3.

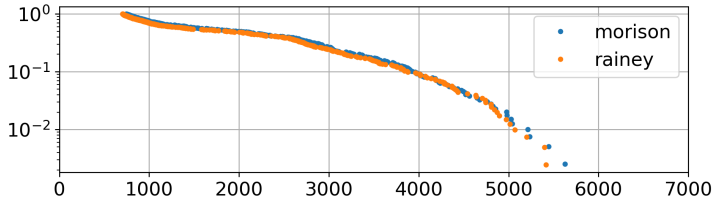

(a) $P_{exc}[-]$ vs. $F_x[kN]$, 1^{st}-order irregular waves

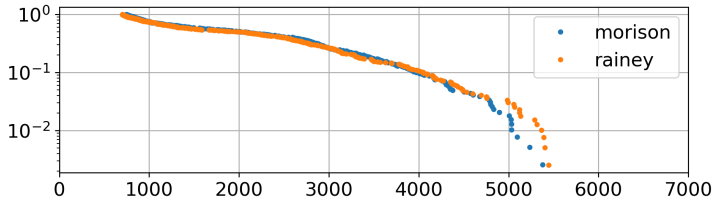

(b) $P_{exc}[-]$ vs. $F_x[kN]$, 2^{nd}-order irregular waves

Figure 3: Exceedance probability of the in-line force peaks at the mudline, measured in kN ($s = 20$, $H_S = 5.5\ m$, $T_P = 9.5\ s$, same random phases). With first order kinematics, the Rainey nonlinear force model and the Morison model predict the same peak statistics. With second order irregular waves, the Rainey model predicts larger extreme values than the Morison force model. The magnitude of the highest peaks in the second order realization is very similar to the amplitude of the first order peaks.

Using second-order irregular waves seems to have little effect on the total damage, as demonstrated by the damage values in LC4 and LC5. According to the exceedance probability plots in Figure 3b and Figure 3a ($H_S = 5.5\ m$), larger peaks are more likely to happen when second order waves are used. However, this difference is not enough to impact the overall fatigue lifetime, also considering that the sea states with the highest H_S have a very low joint probability of occurrence (Figure 2).

When increasing the spread of the spectrum, the overall damage caused by the x-wise mudline force on the pile is smaller. This is as expected, since in a directionally spread spectrum a significant part of the energy comes from the y direction, reducing the x-wise force. Again, using the McCamy-Fuchs force model leads to a reduced fatigue due to the cylinder diffraction. Slender body models predict the same amount of total damage, independently of the wave model used.

It is interesting to note that the total damage due to the flapwise blade root moment is independent of the wave kinematics and wave load model used. This means that the flapwise rotor load is dominated by the aerodynamic loads. Moreover, the high aerodynamic damping acting on the rotor during normal operation is likely suppressing any excitation of the rotor eigenfrequencies.

3.2. Higher-Order modeling of the diffraction around a surface piercing cylinder: linear solver
In this section, we will present some results of the validation of the linear force predicted by the spectral method. The picture and the formulas are reproduced, with permission, from a previous publication [12].

To explain the basic idea behind the solver, we note that the total wave elevation η and velocity potential ϕ for any problem concerning a wave hitting a structure can be written as:

$$\begin{pmatrix}\eta\\ \phi\end{pmatrix} = \begin{pmatrix}\eta\\ \phi\end{pmatrix}_I + \begin{pmatrix}\eta\\ \phi\end{pmatrix}_{D1} + \begin{pmatrix}\eta\\ \phi\end{pmatrix}_{D2} \tag{3}$$

In the equation, the subscript I stands for incoming wave, $D1$ is the first order diffraction potential, while $D2$ is the nonlinear diffraction potential. In cylindrical coordinates (r, θ, z), the z-axis points upwards from the mean sea level at the cylinder centerline, while $\theta = 0$ is the main wave direction.

To be able to represent a generic linear field in cylindrical coordinates, we can think of the wave elevation and potential as a Bessel expansion in the radial direction, and as a cosine expansion in the tangential direction:

$$\eta_I(r,\theta) = \sum_{p=0}^{P}\sum_{j=1}^{N} A_{pj} J_p(k_{pj} r)\cos(p\theta)$$
$$\phi_I(r,\theta,z) = \sum_{p=0}^{P}\sum_{j=1}^{N} B_{pj} J_p(k_{pj} r)\cos(p\theta)\frac{\cosh(k_{pj}(z+h))}{\cosh(k_{pj}h)}$$

The coefficients A_{pj} represent the amplitude of the p^{th} harmonic in the tangential direction, associated with the j^{th} wave number. The radial variation can therefore be described as the J_p Bessel function of the first kind, while the tangential variation is a simple cosine function. The A_{pj} can be retrieved, for example, by a Bessel transform applied in cascade after a cosine transform.

The I plus the $D1$ field from a cylinder of radius r_0 can be written in cylindrical coordinates as an expansion of Bessel Functions in a domain $[r_0, r_{\max}]$, in the same fashion as in the exact linear solution by McCamy and Fuchs:

$$\eta_{ID1} = \sum_{p=0}^{P}\sum_{j=1}^{N}\left[A_{pj}J_p(k_{pj}r) - \Re\left\{\left(A_{pj} + \frac{\mathrm{i}\omega_{pj}}{g}B_{pj}\right)\frac{J'_{pj}}{H'_{pj}}H_p^{(1)}(k_{pj}r)\right\}\right]\cos(p\theta) \tag{4}$$

$$\phi_{ID1} = \sum_{p=0}^{P}\sum_{j=1}^{N}\left[B_{pj}J_p(k_{pj}r) - \Re\left\{\left(B_{pj} + \frac{\mathrm{i}g}{\omega_{pj}}A_{pj}\right)\frac{J'_{pj}}{H'_{pj}}H_p^{(1)}(k_{pj}r)\right\}\right]\cos(p\theta)\frac{\cosh(k_{pj}(z+h))}{\cosh(k_{pj}h)} \tag{5}$$

where $k_{pj}/r_{\max}$ is the j'th root of the first kind Bessel function of order p; $H_p^{(1)}$ is the first kind order p Hankel function; $J'_{pj} \equiv \partial_r J_p(k_{pj}r)|_{r=r_0}$ and $H'_{pj} \equiv \partial_r H_p^1(k_{pj}r)|_{r=r_0}$. The J-terms represent the incoming wave in cylindrical coordinates (I). The Hankel functions H are outward propagating waves representing the first order diffracted field $D1$, which is the same as we find in the linear diffraction solution. The coefficients of the Hankel functions are derived from impermeability boundary condition on the cylinder wall.

The explanation of the derivation of the nonlinear potential $D2$ is out of the scope of the present description, and will be subject of a future publication currently under preparation.

A first important validation is that the theory is consistent with linear diffraction from McCamy and Fuchs when the cylinder is exposed to a linear monochromatic wave. The McCamy-Fuchs analytical solution for the force on a cylinder of radius r_0 exposed to a wave with wave number k and positioned at water depth h is the following:

$$F = \frac{2\rho g H}{k^2}A(kr_0)\tanh(kh)\cos(\omega t - \delta(kr_0)) \tag{6}$$

where $A(kr_0) = \left[J_1'(kr_0)^2 + Y_1'(kr_0)^2\right]^{-1/2}$, Y_1 is the first order Bessel function of second kind and $\delta(kr_0)$ is a phase shift. Figure 4 shows the value of $A(kr_0)$ as obtained by the spectral method, compared to the analytical solution. A perfect match is seen for the various values of kr_0.

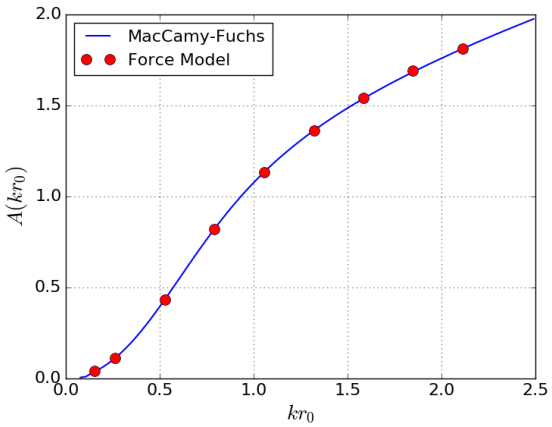

Figure 4: Magnitude of the first order force predicted by the spectral solver versus the McCamy and Fuchs analytical solution, adapted with permission from figure 2 in [12]

3.3. CFD modeling of loads on a stiff cylinder

CFD computations on stiff cylinder were used to help the validation of engineering models in the most complex cases. One important result is relative to loads on stiff cylinders caused by nonlinear waves. In the framework of the Danish WaveLoads project [28], DTU measured the inline force on a stiff cylinder positioned on a shoaling slope (1:25), subject to regular waves of different height. The experiments were reproduced in DIMSELO, both via accurate CFD viscous computations and by 3DFloat [14]. The high fidelity CFD model resolved the fluid domain around the cylinder with a total of 500'000 cells. The 3DFloat model used streamfunction regular waves and the above mentioned Rainey force model. Figure 5 shows the inline force on a stiff cylinder, with a diameter of $D = 0.075\ m$, exposed to two different sets of regular waves. In Figure 5a, the 3DFloat force computations match the experiments very closely, and so do the CFD computations. For a high steepness wave, in Figure 5b, differences start to arise. A secondary load cycle appears close to the trough of the experimental force timeseries, caused by a local diffraction happening on the back side of the cylinder. Since the wave model used for the aeroelastic computations does not include any modification of the waves due to the presence of the structure, the deriving force signal struggles to follow the experimental one. On the other hand, the CFD model handles the surface diffraction correctly, and is able to reproduce the experimental signal very closely.

4. Conclusion

DIMSELO has been successful in analyzing the effect of improved physical modeling of offshore wind turbines. Through advanced CFD, it was possible to analyze the nonlinear loads around a cylinder in regular and irregular waves. An innovative spectral potential solver to calculate nonlinear loads on offshore structures was developed at DTU. The model showed to be a promising alternative to CFD for calculating nonlinear loads on piles, and requires a fraction of the computational cost.

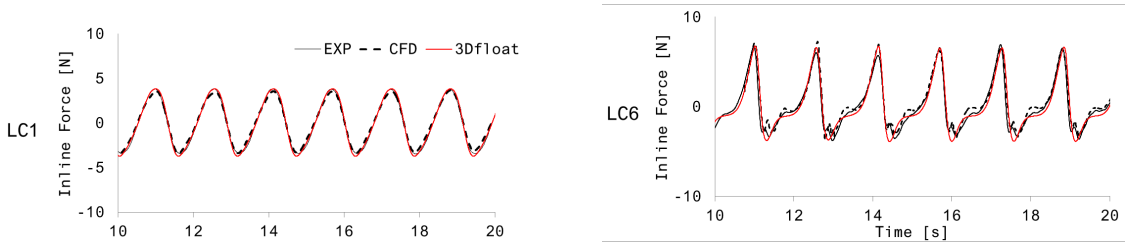

(a) Linear wave, $H = 0.09\ m$,$T = 1.56\ s$ (b) Nonlinear wave, $H = 0.15\ m$,$T = 1.56\ s$

Figure 5: Comparison of computations with STAR-CCM (CFD), experiments from the WaveLoads project (Exp) and computations via the aeroelastic code 3DFloat. Reproduced from figure 15 in [14]

The results presented this paper have showed the consequences of enabling more physically complete engineering models in aeroelastic calculation of fatigue design loads on a bottom fixed 10 MW offshore turbine. In particular, using a load model which captures first order diffraction predicts a 15% lower total fatigue damage induced by streamwise force at the mudline. Using second order irregular waves and nonlinear force models did not have a significant impact on the fatigue loads. This means that in some particular cases nonlinearities can be neglected when computational speed and ease of use are a critical factor. Also, blade flapwise loads were insensitive to the wave load model.

A final report for DIMSELO will be available in the first half of 2018, where the impact of the computational modes on the whole design of the three above mentioned structures will be presented.

5. Funding and acknowledgments

The work was funded for 80% by the Norwegian Research Council, through the ENERGIX program. The remaining 20% was funded jointly by Statoil and Statkraft. We deeply acknowledge Tor David Hansen from Statoil for his technical support through the project, and for providing typical soil and met-ocean data for a typical Northern Sea location.

References

[1] Sharma J, Dean R *et al.* 1981 *Society of Petroleum Engineers Journal* **21** 129–140
[2] Engsig-Karup A P, Bingham H B and Lindberg O 2009 *J. Comput. Phys.* **228** 2100–2118
[3] Morison J, Johnson J, Schaaf S *et al.* 1950 *Journal of Petroleum Technology* **2** 149–154
[4] McCamy R and Fuchs R 1954 Wave forces on piles: a diffraction theory Tech. rep. US Army Corps of Eng.
[5] Larsen T J and Hansen A M 2007 How2 hawc2 (user manual) Tech. rep. DTU Wind Energy
[6] Reinholdtsen S and Falkenberg E 2001 Simo (user manual) Tech. rep. MARINTEK
[7] IEC 2009 Wind turbines - part 3: Design requirements for offshore wind turbine
[8] Haver S and Winterstein S R 2009 *Transactions of the Society of Naval Architects and Marine Engineers* **116** 116–127
[9] Nygaard T A, De Vaal J, Pierella F, Oggiano L and Stenbro R 2016 *Energy Procedia* **94** 425–433
[10] Pierella F, Stenbro R, Oggiano L, de Vaal J, Nygaard T A, Krokstad J *et al.* 2017 *Proceedings of the 27th International Ocean and Polar Engineering Conference* (ISOPE)
[11] Rainey R 1995 *Proceedings of the Royal Society of London. Series A: Mathematical and Physical Sciences* **450** 391–416
[12] Bredmose H and Andersen S J 2017 *Proceeding of the 32nd International Workshop on Water Waves and Floating Bodies*
[13] Oggiano L, Pierella F, Nygaard T A, Vaal J D and Arens E 2017 *Energy Procedia* **137** 273 – 281 ISSN 1876-6102
[14] Oggiano L, Pierella F, de Vaal J, Nygaard T A, Stenbro R, Arens E *et al.* 2016 *Proceedings of the 26th International Ocean and Polar Engineering Conference* (ISOPE)

[15] Oggiano L, Pierella F, De Vaal J, Nygaard T A, Stenbro R, Arens E *et al.* 2017 *Proceedings of the 27th International Ocean and Polar Engineering Conference* (ISOPE)
[16] Eliassen L and Obhrai C 2016 *Energy Procedia* **94** 388–398
[17] Eliassen L and Bachynski E E 2017 *ASME 2017 36th International Conference on Ocean, Offshore and Arctic Engineering* (American Society of Mechanical Engineers) pp V010T09A062–V010T09A062
[18] Bak C, Zahle F, Bitsche R, Kim T, Yde A, Henriksen L C, Hansen M H, Blasques J P A A, Gaunaa M and Natarajan A 2013 The dtu 10-mw reference wind turbine Tech. rep. DTU Wind Energy
[19] Eliassen L and Andersen S 2016 *Journal of Physics: Conference Series* vol 753 (IOP Publishing) p 032040
[20] DNV 2010 Dnv-os-j101: Design of offshore wind turbine structures
[21] Hansen M H and Henriksen L C 2013 Basic dtu wind energy controller Tech. rep. DTU Wind Energy
[22] Hansen M O 2015 *Aerodynamics of wind turbines* (Routledge)
[23] DNV 2007 Dnv-rp-c205: Environmental conditions and environmental loads
[24] Mann J 1998 *Probab. Eng. Mech.* **13** 269–282
[25] IEC 2005 Wind turbines part 1: Design requirements (iec 61400-1)
[26] Manners W and Rainey R 1992 *Proceedings of the Royal Society of London. Series A: Mathematical and Physical Sciences* **436** 13–32
[27] Schløer S, Bredmose H and Ghadirian A 2017 *Proceeding of the ASME 2017 36th International Conference on Ocean, Offshore and Arctic Engineering* (ASME)
[28] Bredmose H, Mariegaard J, Paulsen B, Jensen B, Schløer S, Larsen T, Kim T and Hansen A 2013 The wave loads project Tech. rep. DTU Wind Energy